J. Fluid Mech. (2011), *vol.* 674, *pp.* 408–432.
doi:10.1017/S0022112011000012

Three-dimensional vortex dynamics in oscillatory flow separation

MIGUEL CANALS[1]† AND GENO PAWLAK[2]

[1]Department of Engineering Science and Materials, University of Puerto Rico, Mayagüez, PR 00681, USA

[2]Department of Ocean and Resources Engineering, University of Hawaii, Honolulu, HI 96822, USA

(Received 10 August 2009; revised 30 November 2010; accepted 3 January 2011; first published online 23 March 2011)

The dynamics of coherent columnar vortices and their interactions in an oscillatory flow past an obstacle are examined experimentally. The main focus is on the low Keulegan–Carpenter number range ($0.2 < KC < 2$), where KC is the ratio between the fluid particle excursion during half an oscillation cycle and the obstacle size, and for moderate Reynolds numbers ($700 < Re_v < 7500$). For this parameter range, a periodic unidirectional vortex pair ejection regime is observed, in which the direction of vortex propagation is set by the initial conditions of the oscillations. These vortex pairs provide a direct mechanism for the transfer of momentum and enstrophy to the outer region of rough oscillating boundary layers. Vortices are observed to be short-lived relative to the oscillation time scale, which limits their propagation distance from the boundary. The instability mechanisms leading to vortex decay are elucidated via flow visualizations and digital particle image velocimetry (DPIV). Dye visualizations reveal complex three-dimensional vortex interactions resulting in rapid vortex destruction. These visualizations suggest that one of the instabilities affecting the spanwise vortices is an elliptical instability of the strained vortex cores. This is supported by DPIV measurements which identify the spatial structure of the perturbations associated with the elliptical instability in the divergence field. We also identify regions in the periphery of the vortex cores which are unstable to the centrifugal instability. Vortex longevity is quantified via a vortex decay time scale, and the results indicate that vortex pair lifetimes are of the order of an oscillation period T.

Key words: coastal engineering, separated flows, vortex breakdown

1. Introduction

Oscillating flows past bluff bodies are often characterized by coherent vortex structures which have a profound effect on the turbulence dynamics. A classical example is the interaction of an oscillating flow with a cylinder with its axis orthogonal to the flow velocity. If the oscillation amplitude is large with respect to the cylinder diameter, flow separation and vortex shedding occurs, frequently leading to vortex pair formation (Graham 1980). In the coastal ocean, similar dynamics occur during the interaction between the oscillating flows caused by surface gravity waves and

† Email address for correspondence: miguelf.canals@upr.edu

the rippled seabed (Mei & Liu 1993). It is widely accepted that vortex shedding is a dominant process in sediment transport (Mei & Liu 1993). Coherent vortices can suspend sediment into the water column, and this sediment may then be transported by currents. Depending on the flow parameters, vortices may be shed during both stages of the oscillatory flow and may pair up into vortex dipoles. While a large body of work has concentrated on quantifying the associated sediment transport, a detailed study into the three-dimensional (3-D) structure and dynamics of these vortices has been lacking. The present paper is a first step towards increasing our understanding of the 3-D vortex dynamics.

The two-dimensional (2-D) problem was studied analytically by Longuet-Higgins (1981), who found that vortex pairs could escape away from the region where vorticity is generated. Full-scale observations of vortex generation over movable sediment ripple beds have confirmed the presence of intense coherent vortices (Nichols & Foster 2007). Williams *et al.* (2007) conducted laboratory observations for waves over vortex ripples with height h and found that vortex pairs can suspend sediment up to heights of $10h$ above the seabed. These coherent vortices also strongly influence the structure of the bottom boundary layer, since their formation provides a direct convective mechanism for momentum transfer to the outer region of the boundary layer. Experimental results have suggested that their dynamics can directly set the height of rough oscillating boundary layers (Krstic & Fernando 2001). Scandura, Vittori & Blondeaux (2000) investigated the onset of three-dimensional structures in oscillating flows past vortex ripples for moderate Reynolds numbers, by means of direct numerical simulation (DNS). They found that coexisting mushroom (Görtler) vortices and vortices with spanwise coherence quickly lead to a strongly nonlinear turbulent flow. Blondeaux, Scandura & Vittori (2004) conducted DNS of oscillating flow past vortex ripples at low to moderate Reynolds numbers and also noted the complex three-dimensionality of the flow. They showed the existence of streamwise ribs in the strain-dominated regions, which would then wrap around the main spanwise vortex tubes. These studies have shed light on the abundance of 3-D structures in oscillating flows past vortex ripples, but have not directly addressed the question of how the main spanwise vortices lose their coherence.

In realistic vortex-dominated oscillating flows, nominally 2-D vortices quickly develop a complex three-dimensional structure and are short-lived. The process by which these vortices decay so effectively and systematically suggests that some fundamental, repeatable mechanisms are at play. Columnar distributions of vorticity have been extensively studied for well over a century. Since the seminal study of Kelvin (1880), it is well known that columnar vortices can act as waveguides (Chandrasekhar 1981). He investigated analytically the inviscid linear behaviour of a Rankine vortex, with a circular cross-section, to 3-D infinitesimal perturbations, and found them to be neutrally stable. The addition of a strain field, however, can cause instability. A theoretical analysis of the instability of idealized strained vortices to short waves, of the order of the vortex core size, was carried out by Moore & Saffman (1975) and Tsai & Widnall (1976). They found that instability occurs for wavenumbers that result in non-rotating, stationary waves on the vortex, which allows them to become tuned to the strain field acting on the vortex columns. The same type of instability also affects the flow within a rotating cylinder when a strain is imposed on the flow by deforming the cylinder (Eloy, Le Gal & Le Dizès 2000). This strain-induced short-wave instability is now better known as the elliptical instability, and is a generic mechanism in which the resonant interaction between two inertial waves, with azimuthal wavenumbers $m_1 = m$ and $m_2 = m \pm 2$, and an underlying strain field lead to exponential growth

of perturbations on a vortex column. Other instabilities such as the centrifugal instability are also known to destabilize vortex columns (Bayly 1986; Sipp & Jacquin 2000).

The present article is concerned with the three-dimensional dynamics of the coherent vortices present in an oscillatory, fully separated flow. Our experiments have been designed to examine the fundamental features of such flows in an idealized setting. These features include vortex pair formation and the periodic generation of new vortices with spanwise coherence at each half-cycle. In § 2, we describe the experimental set-up and the flow visualization techniques. In § 3, we examine the large-scale vortex dynamics and the associated vortex pair formation. The vortex instability mechanisms are elucidated in § 4 using flow visualizations and velocity measurements, and the results are then interpreted using existing hydrodynamic instability theories, with a focus on the qualitative features of the problem. The nonlinear dynamics and the transition to turbulence are examined in § 5. Vortex evolution is quantified via a vortex decay time scale in § 6, and concluding remarks are given in § 7.

2. Experimental set-up and analysis

2.1. *Laboratory set-up*

Experiments were conducted in a Plexiglas tank with dimensions of $2.1 \times 1 \times 0.6\,\mathrm{m}^3$, with optical access available from all sides and with water as the working fluid. A sketch of the experimental set-up is shown in figure 1. A stepper motor and pulley system was developed to create smooth oscillations of an idealized boundary in an otherwise still fluid. The boundary consisted of a smooth Plexiglas plate with a flap of length η attached orthogonal to the plate. The plate was 1.6 m long and 0.6 m tall, with just enough clearance to enable oscillations of the flap, which ranged in size from $\eta = 2$ to 10 cm. The boundary was painted black to avoid laser reflections and increase the resolution of the velocity measurements close to the boundary, so that the unsteady dynamics of the separating shear layer could be adequately resolved. The vortices resulting from oscillatory flow separation had aspect ratios (height/diameter) of about 30–65. Experiments were designed to isolate the fundamental vortex dynamics and avoid end effects on the dynamics of the vortex columns. The no-slip condition at the top and bottom boundaries can induce axial flows which can propagate as vortex shocks and subsequently lead to vortex breakdown. For most experimental runs, no modifications were needed since the time scale for boundary-induced vortex breakdown was much larger than the time scale for the development of the instabilities which are the subject of this article. This difference in time scales was determined from dye visualizations which will be described below. For some cases, a 5 cm layer of dense salt water ($\rho \approx 1150\,\mathrm{kg\,m^{-3}}$) was added to dampen the vortex shocks as well as the turbulence which was created at the 3 mm wide junction between the bottom Plexiglas wall and the moving boundary.

The oscillation mechanism consisted of a computer-controlled stepper motor connected to a pulley system attached to the moving boundary, which rested on linear bearings enabling smooth movements. A sinusoidal function $U(t) = U_0 \sin[(2\pi/T)t]$ was approximated using a piecewise continuous signal in 0.02 s time steps using a computer interface which controlled the motor via serial commands. The oscillation period, T, was varied from 1 to 4 s, and typical values for U_0 ranged from 1.5 to $6\,\mathrm{cm\,s^{-1}}$, leading to values of the Keulegan–Carpenter number, defined as $KC = (U_0 T)/(\pi\eta)$, from $0.2 < KC < 2$.

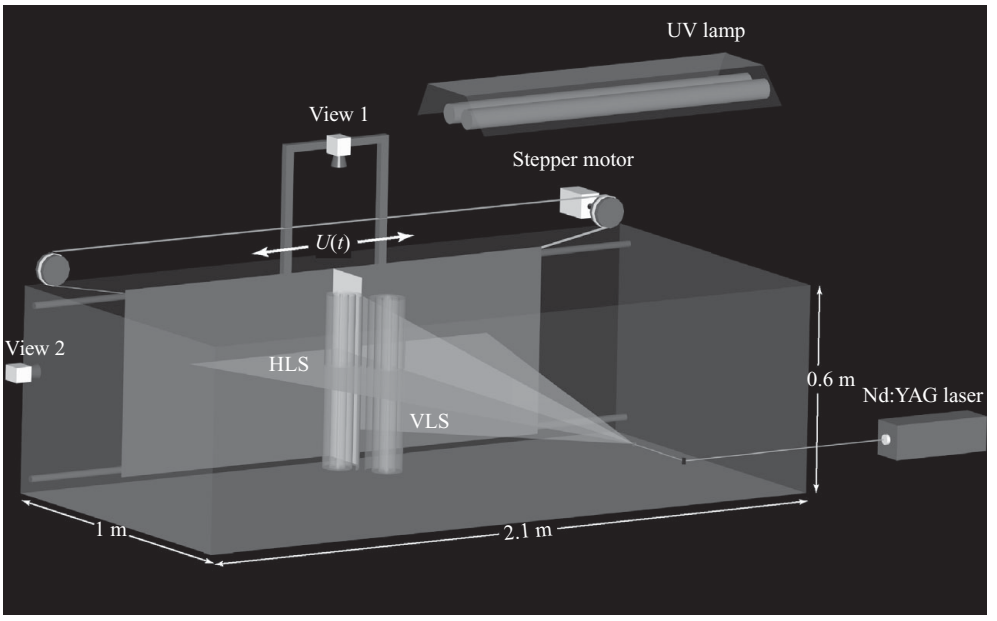

FIGURE 1. Overview of the experimental set-up. The UV lamp was used for volumetric visualizations using UV-induced fluorescence (UVIF). The Nd:YAG laser was used for digital particle image velocimetry (DPIV) measurements. View 1 corresponds to DPIV measurements of the spanwise vorticity with an HLS. A vertical laser sheet (VLS) was used in view 2 to examine the axial structure of the vortices and their horizontal vorticity. A counter-rotating vortex pair is sketched.

2.2. *DPIV measurements*

Velocity measurements were obtained using digital particle image velocimetry (DPIV). A double-pulsed Nd:YaG laser was used to produce a laser sheet to illuminate the flow, which was seeded with reflecting particles. The particles used were Sphericel hollow glass spheres, with diameter ranging from 11 to 18 μm and a density of approximately $1.1\,\mathrm{g\,cm^{-3}}$. These particles were small enough with respect to the scales of the flow (∼1–5 cm) so as to correctly follow the flow under examination. Image pairs were acquired with a high-resolution digital camera (Pixelfly QE, Cooke Corp.) of 1392×1024 pixels, separated by a time interval Δt. The optimal Δt, corresponding to the separation between subsequent laser pulses, was determined from the expected maximum velocity gradients of the flow (Meunier & Leweke 2003). A cross-correlation algorithm was then employed to obtain velocity fields from the image pairs (Fincham & Spedding 1997). Interrogation windows of 32×32 pixels were used, with 50 % overlap (16 pixel spacing), resulting in velocity fields of 86×60 vectors. A five-point median filter was applied to this velocity field to eliminate any spurious vectors. An open-source MATLAB package, DPIVsoft (Meunier *et al.* 2004), was used to carry out the computations using an improved DPIV algorithm, developed by Meunier & Leweke (2003), for flows with high velocity gradients.

Two planes were used to obtain velocity measurements, one orthogonal and one parallel to the spanwise vortex tubes, as sketched in figure 1. The horizontal laser sheet (HLS) was used to resolve spanwise vorticity, and images were obtained with the laser sheet located at mid-depth ($z \approx 27.5$ cm). The camera was attached to the moving Plexiglas plate so that the velocity measurements were obtained in a reference

frame fixed with respect to the oscillating boundary. For this plane, a laser sheet thickness of 3 mm was used so that the highest velocity gradients could be adequately resolved. Typical values of Δt for this plane ranged from 3 to 12 ms, depending on the expected flow velocities.

A vertical laser sheet (VLS) was used to obtain measurements of horizontal vorticity. For some experiments the laser sheet thickness for this plane was increased slightly to 4 mm to reduce the in-plane loss of particle pairs, since the largest velocity component was the out of plane velocity, and values of Δt ranged from 2 to 10 ms. For the VLS, the frame of reference was not fixed to the oscillating boundary, but moved sinusoidally relative to the flap, since the boundary moved back and forth and the laser sheet stayed fixed. Experiments were started with the laser sheet parallel to the flap, and the phase at which the velocity fields were taken was determined from fitting a sinusoid with an oscillation period obtained from Fourier analysis of the spatially averaged velocity.

The repeatable aspects of the vortex dynamics were examined using phase averaging. Velocity fields from at least 20 cycles, ignoring the first cycle, were sorted into bins of 0.2 radians and averaged. At a sampling frequency of 3.3 velocity fields per second, and for the typical periods of the oscillations, a total of 150–400 velocity fields were used to obtain the phase-averaged flow structure of a single cycle. The end result is a periodic 2-D velocity field which is representative of the robust structures of the flow.

2.3. *Dye visualizations*

The three-dimensional structure of the coherent vortices was visualized via UV-induced fluorescence (UVIF). The blacklight beam from a 400 W super-high output UV cannon (American DJ) was directed at the area of interest from a distance of 2 m. Two-colour UVIF was produced using fluorescein and rhodamine-B dyes. The dye was released as a line source by using a cotton thread saturated with the respective dyes, with the thread embedded into thin slits carved on the surface of the flap, positioned slightly upstream from the separation point. In the separated flow, the resulting scalar field can be interpreted as red (green) dye corresponding to positive (negative) vorticity, although this is only valid in a qualitative sense. Only the first three cycles could be photographed before the dye fully covered the volume of interest, making further visualizations impossible. The vortices produced during the first cycle were not considered since they are subject to transient effects that do not adequately represent the periodically generated structures which are the focus of this article. The initial vortex pairs also propagated in different directions than those on subsequent cycles, usually towards the boundary at $y/\eta = 0$.

2.4. *Relevant length scales*

For a typical run, a representative vortex core size, a, was obtained from a nonlinear least-squares fitting algorithm, which fits an elliptical Gaussian vortex patch of the form

$$\omega_{ls} = \omega_0 \exp\left\{\left(\frac{(x-x_0)\cos\varsigma - (y-y_0)\sin\varsigma}{L_A}\right)^2 + \left(\frac{(x-x_0)\sin\varsigma - (y-y_0)\cos\varsigma}{L_B}\right)^2\right\} \quad (2.1)$$

to the vorticity data, where ς is the angle of rotation of the semi-major axis of the vortex with respect to the x-axis. The parameters $\{x_0, y_0, L_A, L_B, \omega_0, \varsigma\}$ were obtained

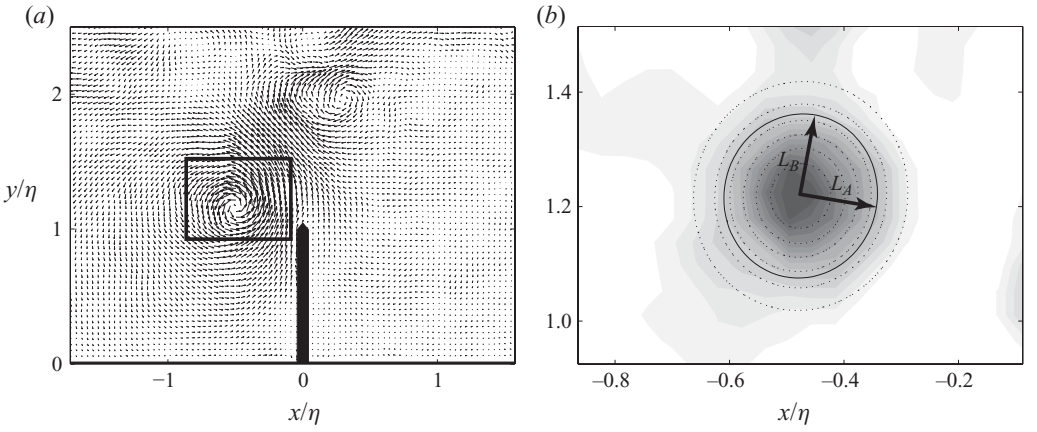

FIGURE 2. Typical DPIV results for a vortex pair and relevant length scales for the highest Reynolds number case, $Re_v = 7200$. (*a*) Velocity field of 86×60 vectors showing vortex pair propagation at an angle close to 45° to the free stream. Note the strong jet inclined at the same angle. (*b*) The filled contours represent the vorticity of the rectangular region in (*a*), and the dashed contours represent the least-squares fit using a Gaussian elliptical vortex with maximum vorticity ω_0 (given by the darkest shade of grey). The solid line represents the *e*-folding vorticity contour, and the length scales L_A and L_B are sketched.

from the fitting algorithm. The equivalent core size is then given by $a = \sqrt{L_A L_B}$ and corresponds to the core radius a of a Lamb–Oseen vortex when $L_A = L_B$, in which case the maximum vorticity is given by $\omega_0 = \Gamma/(\pi a^2)$. The scale, a, was obtained from the vortex cores once the shear layer was completely rolled up into a coherent vortex. From the vorticity scale, ω_0, and the equivalent core size, a, the vortex circulation, Γ, can be obtained, and a vortex Reynolds number can be defined as $Re_v = \Gamma/\nu$. From the coordinates of the vortex centre, the distance, b, between two vortices in a given pair can be obtained.

In figure 2, we show typical DPIV results obtained in the HLS for $Re_v = 7200$ and $KC = 0.42$. The velocity field is shown in figure 2(*a*), showing a vortex pair propagating away from the boundary at an angle close to 45°. In figure 2(*b*), we show the vorticity field for the rectangular region outlined in figure 2(*a*), with darker shading indicating stronger positive vorticity. The dashed lines correspond to the vorticity contours for a least-squares fit of the elliptical Gaussian vortex (defined by (2.1)) to the vorticity data. The solid line corresponds to the *e*-folding vorticity contour ($\omega_{ls} = \omega_0 \mathrm{e}^{-1}$), which forms an ellipse centred at (x_0, y_0) with its semi-major and semi-minor axes given by L_B and L_A, respectively, and its semi-major axis rotated by an angle ς from the x-axis.

The error associated with this fit is related to the departure of the measured vorticity distribution from the elliptical Gaussian morphology of our model. Errors in the measurements of the vortex core size a can be estimated by comparing the *e*-folding vorticity contour from the DPIV data with the *e*-folding contour from the Gaussian fit to the DPIV data. The area inside the *e*-folding vorticity contour from the experimental data can be used to obtain an equivalent circular vortex core of radius a_c. The error associated with the fit can then be estimated by comparing the value of a from the Gaussian fit with the value of a_c. For each experiment, this error varied from 3% to 9 %.

3. Observations

All experimental runs were carried out at values of KC for which vortex pair formation was expected ($0.2 < KC < 2$). Reynolds numbers ranged from 700 to 7500, at which all vortices were observed to become unstable. The instability mechanisms were robust and will be illustrated via flow visualizations and 2-D quantitative measurements. In this section, we characterize the vortex pair dynamics associated with oscillatory flow separation and examine the 3-D structure of the spanwise vortex tubes.

3.1. *Vortex pair dynamics*

For low KC, vortex pair formation is an important mechanism which has been related to sediment transport and to the energetics of oscillating boundary layers. It has previously been noted that in regular oscillatory flow, vortex pairs will propagate at an angle to the free-stream velocity (Graham 1980). This angle is usually around 30°–60° and varies as a function of KC, depending on the degree of asymmetry of the resulting vortex pairs, as well as the trajectory of the initial vortex of each pair (Tao & Thiagarajan 2003).

In figure 3, we show a sequence of the phase-averaged velocity and vorticity fields from DPIV data for $Re_v = 3800$ and $KC = 1.07$, showing the typical vortex interactions which develop. During one part of the cycle, the shear layer rolls up into a coherent vortex. As the flow turns, another vortex with opposite-signed vorticity forms. The two vortices then pair up and rapidly propagate away from the boundary under mutual advection. It can be seen that coherent vortex pairs propagate to distances of $y/\eta > 2$ from the boundary. For this experiment, the vortex pairs only propagated in the positive x/η direction, and the shedding direction remained stable for all subsequent cycles. The stability of this regular asymmetric mechanism was observed experimentally by Singh (1979). Graham (1980) gave a semi-analytical model of this phenomenon using conformal mapping.

It is notable that the direction of unidirectional vortex pair propagation depends on the initial conditions of the oscillations. For the case shown in figure 3, all vortex pairs propagated in the positive x-direction. For experiments with oscillations starting in the opposite direction, vortex pairs propagated in the negative x-direction. The unidirectional propagation is a well-known feature in regular oscillatory flow, with the memory of the initial conditions retained as $t \to \infty$ (Singh 1979). This unidirectional regime was a robust feature for all the values of KC which were examined ($0.2 < KC < 2$), in agreement with previous studies (Singh 1979; Graham 1980). These strongly asymmetric vortex dynamics can generate asymmetric mean flows due to vortex pair ejection.

Vortex pairs were observed to decay fairly quickly, and only last as coherent structures for about an oscillation period T or less after they propagate away from the boundary. Vortex trajectories were very repeatable for each case and the observed phased-averaged vortex decay is representative of the instantaneous vortex dynamics, as will be demonstrated in § 6. The structures quickly lose coherence and break down into small scales in a repeatable manner, with every pair undergoing the same cycle of pair formation and rapid demise. This suggests that some fundamental 3-D mechanism quickly leads to the loss of spanwise coherence.

3.2. *Observations of three-dimensional structures*

The DPIV measurements shown above suggest rapid vortex destabilization associated with vortex interactions. Figure 4 shows a sequence of the development

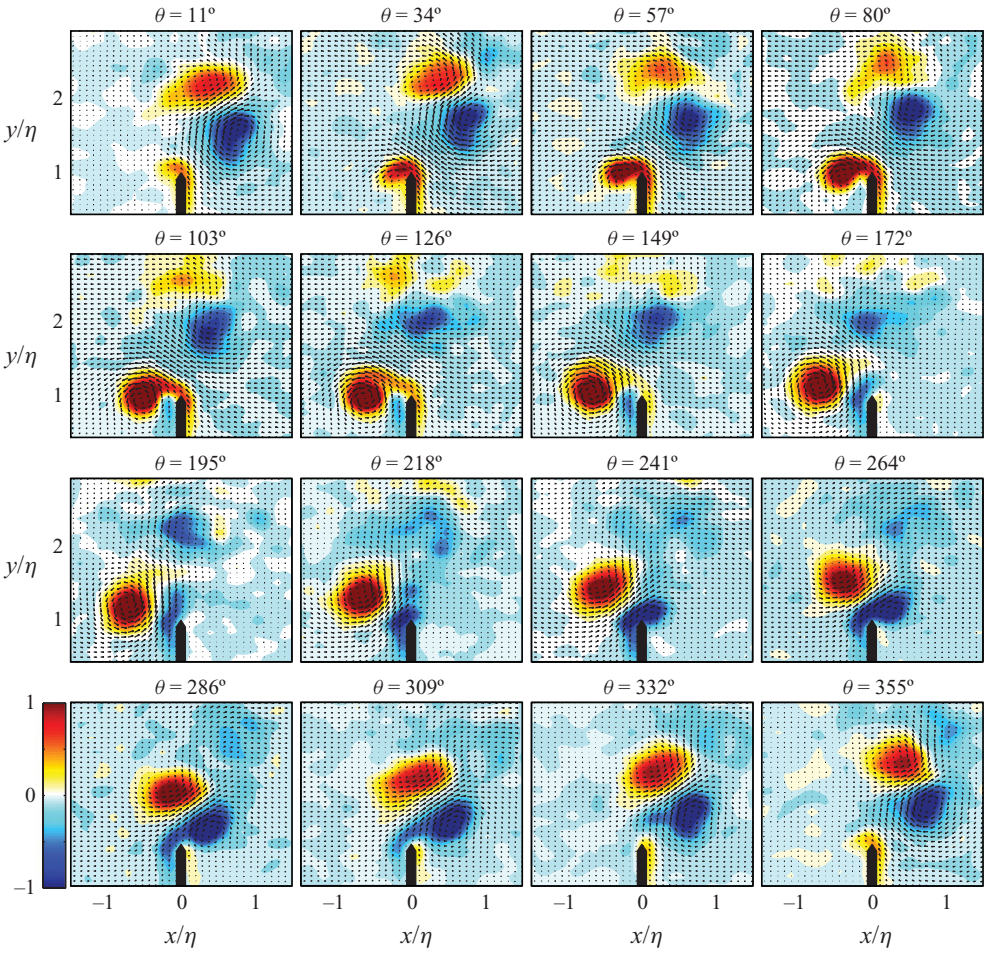

FIGURE 3. Sequence of phase-averaged spanwise vorticity and velocity vectors showing vortex pair formation for $Re_v = 3800$ and $KC = 1.07$. The phase of the oscillation, θ, is given in degrees at the top of each frame. Note the ejection of a single vortex pair in the positive x/η direction, which is a repeatable feature for each cycle.

of three-dimensional structures for $KC = 0.9$ and $Re_v = 1800$. The most recent vortex pair is shown by white arrows in frame *b*. Spanwise undulations can be seen growing in one of the vortices, while a new vortex is forming to its left, leading to the formation of a vortex pair in frame *c*. The remains of the first vortex pair, which has a different trajectory than the initial pair, as described above, can also be seen to the right. Axially periodic perturbations take the form of sinusoidal displacements of the vortex core as well as secondary ring-like structures in the periphery of the vortices. These perturbations quickly grow and break down the vortices, usually in less than an oscillation period after the vortex is fully formed, as suggested by the DPIV measurements of spanwise vorticity shown in figure 3.

3.3. *Wavelength of the observed instabilities*

Before seeking a physical explanation for the instability, it is instructive to examine the dominant wavelengths of the perturbations. The purpose of this simple analysis is to

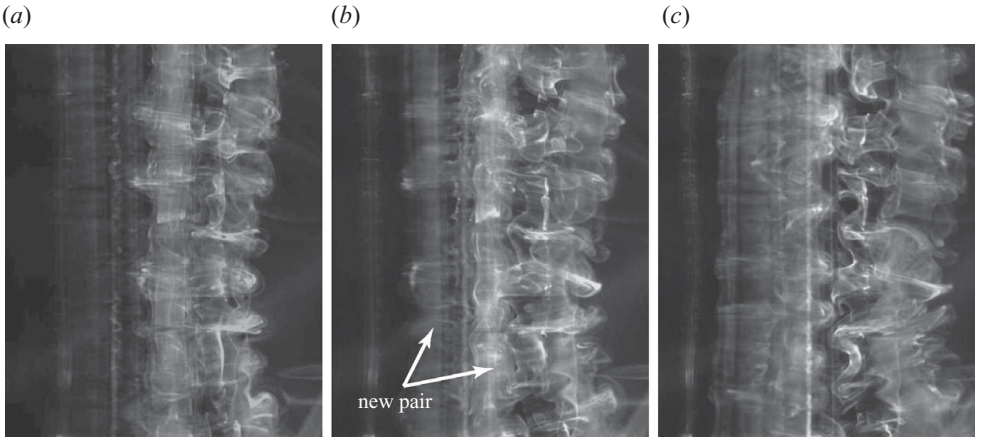

FIGURE 4. Dye visualizations of the onset of three-dimensionality of the spanwise vortex columns for $KC = 0.9$ and $Re_v = 1800$, for the second oscillation cycle at (*a*) $\theta \approx 140°$, (*b*) $\theta \approx 180°$ and (*c*) $\theta \approx 220°$. The arrows in (*b*) point to the most recent vortex pair. To the right of this pair are the remnants of the pair formed in the initial cycle.

measure the axial wavelengths present regardless of the specific instability mechanism causing these perturbations. A measurement of the instability wavelength, λ, may be obtained directly from the spectra of vertical profiles of the velocity magnitude $\sqrt{v^2 + w^2}$ within the perturbed vortex cores, taken using the VLS, as illustrated in figure 5. We define an average core size a for each experiment by taking the mean of all the core sizes of the vortices from the horizontal plane measurements. The radius of each vortex was measured when the vortex was deemed to be fully formed. This was determined as the time at which the vorticity was a maximum over the vortex lifetime. We assume that the vortex radius does not change significantly between that time and the time at which the instability sets in. That time difference was small enough that viscous effects, which would tend to increase the vortex size through diffusion, were considered negligible. The ratio λ/a is shown in figure 5(*d*), with the error bars showing one standard deviation. The observed axial wavelengths are in the range of $2 < \lambda/a < 5$, and there is a decrease in λ/a for increasing Re_v, which is to be expected since as the Reynolds number increases the viscous damping of the smaller scales decreases. In the next section, we will relate these observations to well-defined instability mechanisms.

4. Instability mechanisms

In the preceding section, we saw that the flow is populated by periodic vortices with spanwise coherence which then break down into turbulence. Dye visualizations and DPIV measurements (figures 4 and 5) suggest that instabilities with well-defined axial wavelengths initiate the transition to turbulence. In this section, we analyse what types of instabilities are responsible for this rapid transition to 3-D turbulence.

4.1. *Elliptical instability*

The first candidate for instability we will examine is the well-known elliptical instability of a vortex column subject to a strain field. We are motivated to consider this

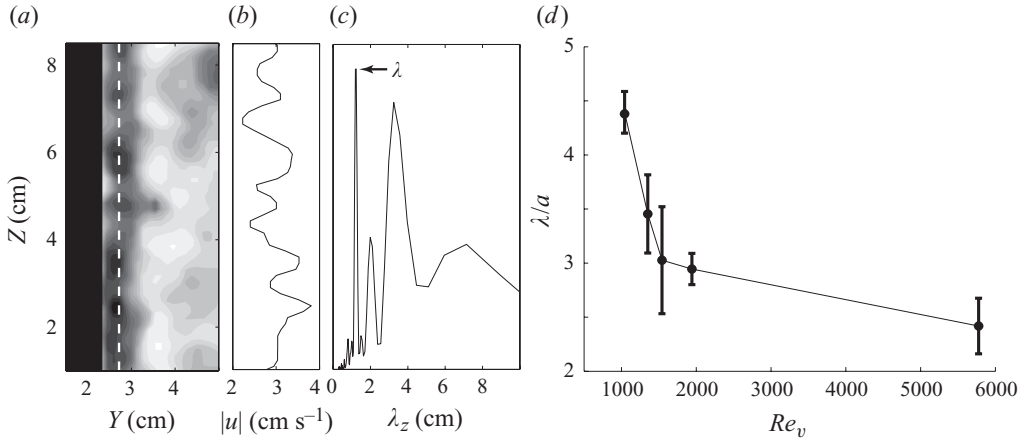

FIGURE 5. Measurements of the instability wavelength from DPIV measurements in the vertical plane. (*a*) Contours of the velocity magnitude $|u| = \sqrt{v^2 + w^2}$ in the vertical plane (VLS). The black rectangle denotes the location of the flap. (*b*) Vertical profile of the velocity magnitude along the white dashed line in (*a*). Note the axially periodic perturbations. (*c*) Spectra of the profile in (*a*). The wavelength of maximum energy represents the dominant axial wavelength λ. (*d*) Non-dimensional wavelength λ/a from DPIV measurements as a function of Re_v. Error bars indicate one standard deviation.

instability due to the strong vortex interactions as seen in figure 3, which usually induce a strain field on the interacting vortices, and the sinusoidal perturbations of the vortex cores seen in the dye visualizations. Here we briefly review the analytical solution given by Waleffe (1990), giving just enough detail to compare our observations with elliptical instability theory. He considered a straight vortex tube immersed in a strain field orthogonal to its axis. The velocity field $\boldsymbol{U}_{2D}$ of the base flow is given by the superposition of solid body rotation around the vertical (z) axis and potential stagnation point flow with stretching in the $-45°$ direction:

$$\boldsymbol{U}_{2D} = -y\left(\frac{\overline{\omega}_z}{2} + \epsilon\right)\hat{\boldsymbol{i}} + x\left(\frac{\overline{\omega}_z}{2} - \epsilon\right)\hat{\boldsymbol{j}}, \tag{4.1}$$

where $\overline{\omega}_z$ is the constant vertical vorticity of the solid body rotation, ε is the uniform strain rate, and $\hat{\boldsymbol{i}}$ and $\hat{\boldsymbol{j}}$ are the unit vectors in the x- and y-directions, respectively. The streamfunction is given by $\psi(\boldsymbol{x}) = -1/2[(\overline{\omega}_z/2 - \varepsilon)x^2 + (\overline{\omega}_z/2 + \varepsilon)y^2]$, and the aspect ratio of the streamlines is given by $E = \sqrt{(\overline{\omega}_z/2 + \varepsilon)/(\overline{\omega}_z/2 - \varepsilon)}$. The streamfunction and strain fields for this flow are shown in figure 6(*a*). Waleffe (1990) linearized the Euler equations about this base flow, and used normal mode perturbations of the form

$$[\boldsymbol{u}', p'] = [f(t), g(t)]\,\mathrm{e}^{\mathrm{i}(\boldsymbol{k}\cdot\boldsymbol{x})} \tag{4.2}$$

where $\boldsymbol{u}'$ and p' are the velocity and pressure perturbations, respectively, $f(t)$ and $g(t)$ represent their respective time dependence and $\boldsymbol{k}$ is the wavenumber vector. A superposition of Fourier modes was carried out by Waleffe (1990) to build localized solutions which maximize the growth rate of the perturbations. In elliptico-polar coordinates ($\boldsymbol{x} = [x, y, z] = [r^* E\cos\theta, r^*\sin\theta, z]$), r^* is constant along a streamline,

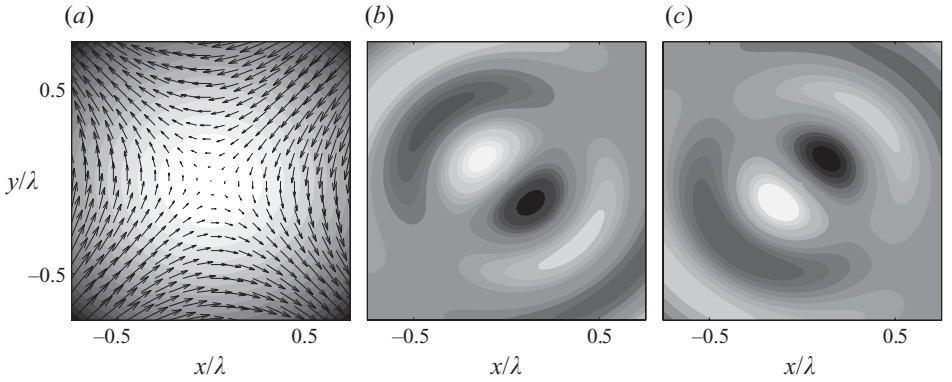

FIGURE 6. Structure of the perturbation fields associated with the elliptical instability of an unbounded vortex with $\bar{\omega}_z > 0$ and $E = 1.2$. (*a*) Streamfunction (shading) and the velocity field associated with the pure straining flow. The stretching direction is inclined at an angle of $3\pi/4$ from the semi-major axis of the ellipse. (*b*) Perturbation vorticity ω_z'. (*c*) Divergence field $\nabla_h \cdot \boldsymbol{u}_h'$ associated with the perturbation. The coordinates have been non-dimensionalized by the axial wavelength λ of the perturbation.

and the perturbation velocity and vorticity fields take the form

$$\boldsymbol{u}' = \begin{Bmatrix} u_{r^*}' \\ u_\theta' \\ u_z' \end{Bmatrix}^{\mathrm{T}} = C\,\mathrm{e}^{\sigma_e t} \begin{Bmatrix} \dfrac{\sqrt{3}}{2}\left[\mathrm{J}_0(\Upsilon) + \dfrac{1}{3}\mathrm{J}_2(\Upsilon)\right]\cos(k_z z)\sin\left(\theta + \dfrac{\pi}{4}\right) \\ \dfrac{\sqrt{3}}{2}\left[\mathrm{J}_0(\Upsilon) - \dfrac{1}{3}\mathrm{J}_2(\Upsilon)\right]\cos(k_z z)\cos\left(\theta + \dfrac{\pi}{4}\right) \\ \mathrm{J}_1(\Upsilon)\sin(k_z z)\sin\left(\theta + \dfrac{\pi}{4}\right) \end{Bmatrix}^{\mathrm{T}}, \tag{4.3}$$

$$\boldsymbol{\omega}' = \begin{Bmatrix} \omega_{r^*}' \\ \omega_\theta' \\ \omega_z' \end{Bmatrix}^{\mathrm{T}} = C\,\mathrm{e}^{\sigma_e t} \begin{Bmatrix} \sqrt{3}k_z\left[\mathrm{J}_0(\Upsilon) + \dfrac{1}{3}\mathrm{J}_2(\Upsilon)\right]\sin(k_z z)\cos\left(\theta + \dfrac{\pi}{4}\right) \\ -\sqrt{3}k_z\left[\mathrm{J}_0(\Upsilon) - \dfrac{1}{3}\mathrm{J}_2(\Upsilon)\right]\sin(k_z z)\sin\left(\theta + \dfrac{\pi}{4}\right) \\ -2k_z\mathrm{J}_1(\Upsilon)\cos(k_z z)\cos\left(\theta + \dfrac{\pi}{4}\right) \end{Bmatrix}^{\mathrm{T}}, \tag{4.4}$$

where J_n corresponds to the nth-order Bessel function of the first kind, $\Upsilon = \sqrt{3}k_z r^*$ is the argument of the Bessel functions, σ_e corresponds to the growth rate of the instability, $k_z = 2\pi/\lambda_z$ is the axial wavenumber and C is a constant. The phase shift of $\pi/4$ which appears in all expressions is due to the fact that the stationary inertial modes are aligned in the direction of extensional strain, so that instability can occur as a result of vortex stretching. In the limit of vanishing strain ($E \to 1$), the growth rate for the elliptical instability is given by $\sigma_e = (9/16)\varepsilon - \nu k_o^2$, where the constant $k_o = 2k_z$ (Landman & Saffman 1987; Waleffe 1990). The viscous correction was given by Craik & Criminale (1986) and corresponds to the viscous damping of individual inertial waves. The spatial structure given by (4.3) and (4.4) has been identified in previous experiments involving vortex columns (Leweke & Williamson 1998; Meunier & Leweke 2005).

4.1.1. *Quantitative observational evidence of the elliptical instability*

We now seek quantitative evidence of the perturbation fields associated with the elliptical instability in the structure of the vortices under investigation. Previous experimental studies have shown good agreement between theory and experiment in idealized open flows such as co-rotating and counter-rotating vortex pairs. Leweke & Williamson (1998) and Meunier & Leweke (2005) used DPIV measurements to extract the perturbation fields associated with the growing elliptical instability in symmetric vortex pairs. They exploited the inherent symmetries and anti-symmetries associated with their base flow to decompose the flow into a background state and the associated perturbation. Their results revealed a very good agreement with the perturbation spanwise vorticity ω_z' given in (4.4), with the perturbation fields aligned in the stretching direction of the strain field. The complexity of the flow in our case does not allow for extraction of perturbation quantities using such symmetry arguments, so we will need to identify perturbation quantities measurable with DPIV. We will exploit the fact that an elliptical vortex column with a purely horizontal velocity field and no spanwise bending has zero divergence of its horizontal velocity field, e.g. $\nabla_h \cdot \boldsymbol{U}_{2D} = 0$, where the subscript h stands for the horizontal component of a vector. The divergence of the velocity field composed of the superposition of an unbounded elliptical vortex column, with its velocity field given by U_{2D} and the perturbation velocity field $\boldsymbol{u}'$ (4.3) associated with the elliptical instability, is given by

$$\nabla_h \cdot \boldsymbol{u}_h = \nabla_h \cdot (\boldsymbol{U}_{2D} + \boldsymbol{u}_h') = -\frac{\partial u_z'}{\partial z} = -Ck_z \, \mathrm{e}^{\sigma_\epsilon t} J_1(\sqrt{3}k_z r^*) \cos(k_z z) \sin\left(\theta + \frac{\pi}{4}\right). \quad (4.5)$$

The structure of the perturbation spanwise vorticity and the divergence field are shown in figure 6. The perturbation spanwise vorticity ω_z' is shown in figure 6(b). Note that the dipolar pattern is aligned with the stretching direction shown in figure 6(a), which is consistent with the vortex core being displaced sinusoidally in that direction. This means that the perturbation vorticity is aligned with the eigenvector of the strain rate tensor that denotes extensional strain, which is the fundamental mechanism leading to vortex stretching and perturbation growth. The divergence field $\nabla_h \cdot \boldsymbol{u}_h'$ is shown in figure 6(c). Note that the pattern shows a $\pi/2$ phase shift with respect to the spanwise vorticity and the stretching direction of the strain field, and this pattern is inclined at an angle $\pi/2$ from the semi-major axis of the elliptical streamlines.

In order to understand the alignment between the coherent patterns in the divergence field with the local flow topology, we consider the structure of the local strain rate tensor $\boldsymbol{S}$. The structure of $\boldsymbol{S}$ can be described in terms of its principal eigenvalues γ, β and χ (where $\gamma > \beta > \chi$) and the corresponding eigenvectors $\boldsymbol{e}_\gamma$, $\boldsymbol{e}_\beta$ and $\boldsymbol{e}_\chi$. For an incompressible flow, we have $\nabla \cdot \boldsymbol{u} = 0$, which requires that $\gamma + \beta + \chi = 0$. If the flow is purely horizontal (2-D), we obtain that $\chi = 0$ and $\gamma = -\beta$, where γ is always positive and denotes extensional strain. Since we only have a 2-D slice of the velocity field from DPIV measurements, our use of $\boldsymbol{S}$ is restricted to the vortex cores, where the flow is assumed to be approximately two-dimensional but weakly divergent. We assume that the principal axes of the strain rate tensor lie approximately in the horizontal plane, and that $\gamma \approx -\beta$, so $\boldsymbol{e}_\gamma$ corresponds to the direction of extensional strain. For the base flow U_{2D} defined in (4.1), with $\overline{\omega}_z > 0$, the eigenvector field $\boldsymbol{e}_\gamma$ at the vortex centre is inclined at an angle of $3\pi/4$ from the semi-major axis of the elliptical streamlines, as can be deduced from figure 6(a). In a realistic vortex which is elliptically unstable, and if the perturbation vorticity were aligned with the strain,

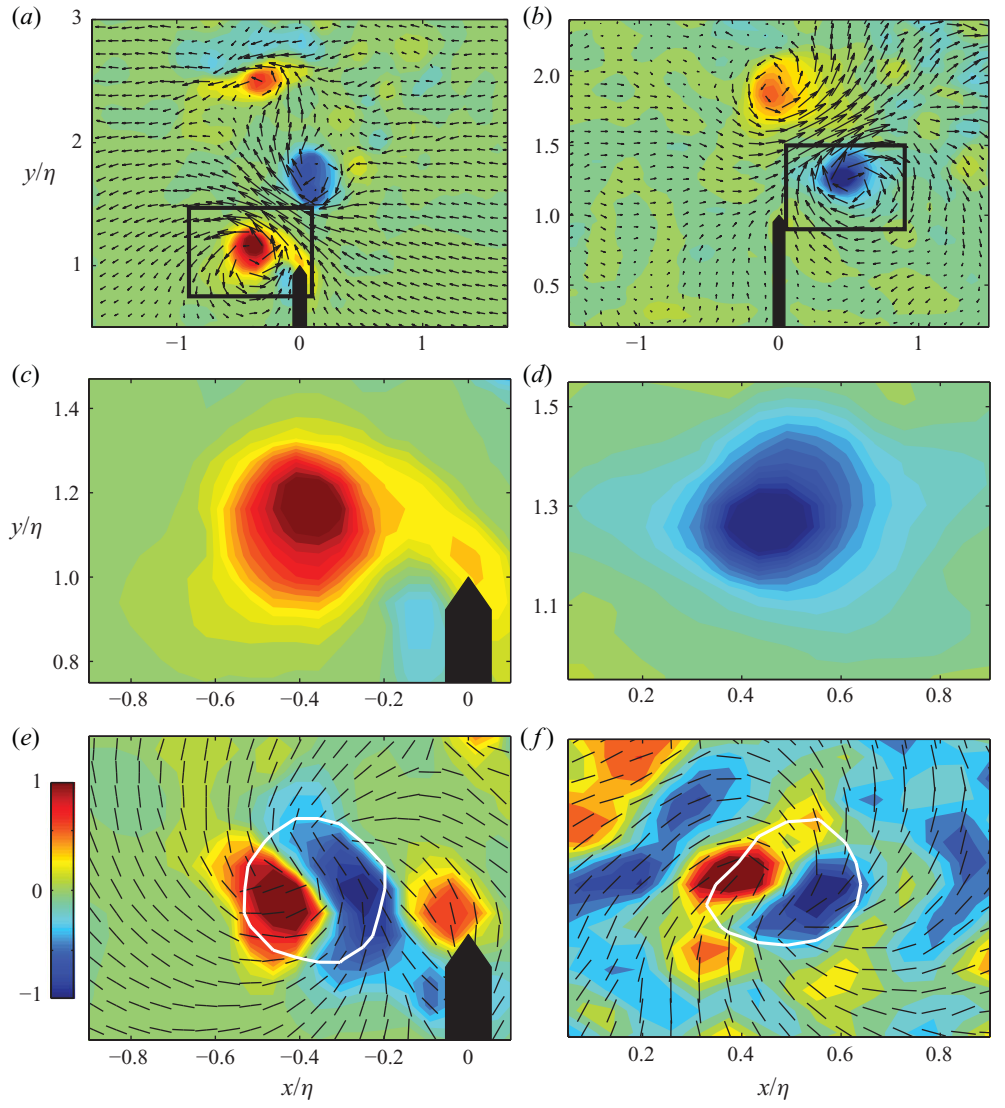

FIGURE 7. Perturbation fields associated with instability as detected from DPIV measurements. (*a*) Velocity and vorticity fields for $KC = 0.91$ and $Re_v = 2300$ at $\theta \approx 180°$ for the eighth cycle. (*b*) Same as in (*a*) but for $KC = 0.42$ and $Re_v = 7200$ at $\theta \approx 350°$ for cycle number 12. Only every other vector has been plotted for visual clarity. (*c*)–(*d*) Vorticity contours of the vortices outlined in (*a*) and (*b*), respectively. (*e*)–(*f*) Eigenvector field $\boldsymbol{e}_\gamma(\boldsymbol{x})$ denoting the local direction of extensional strain, and the divergence field $\nabla_h \cdot \boldsymbol{u}_h$ (contours) of the vortices in (*c*) and (*d*), respectively. The colourbar represents the normalized divergence field shown in (*e*) and (*f*).

we would expect an angle of approximately $\pi/2$ between the eigenvectors $\boldsymbol{e}_\gamma$ in the vortex centre and a perturbation of azimuthal wavenumber 1 in the divergence field.

Figure 7 shows the instantaneous vorticity and divergence fields from DPIV for typical vortex structures for $KC = 0.91$, $Re_v = 2300$ and $KC = 0.42$, $Re_v = 7200$. The velocity and vorticity field at two different phases of the oscillations are plotted in figures 7(*a*) and 7(*b*). The vorticity contours for the vortex with $\omega_z > 0$ (red) outlined in figure 7(*a*) are shown in figure 7(*c*), while the contours for the vortex with $\omega_z < 0$

(blue) in 7(*b*) are shown in 7(*d*). The divergence field and the eigenvectors denoting the direction of local extensional strain for the vortices in figures 7(*c*) and 7(*d*) are shown in figures 7(*e*) and 7(*f*), respectively. We emphasize that the eigenvectors are only an approximation of the direction of the extensional strain within the vortex core, since a non-zero divergence field exists within the core. The divergence field shows a dipolar structure which is remarkably similar to the divergence field shown in figure 6. The patterns are inclined, as expected from the instability theory, at an angle close to $\pi/2$ from the orientation of most of the eigenvectors near the vortex centre. This implies that the vortex core is displaced in the direction of extensional strain, which leads to the stretching of perturbation horizontal vorticity and to the growth of the instability. The white line corresponds to the *e*-folding vorticity contour, and is shown to illustrate the localization of the perturbation field within the vortex core. This localization agrees with the numerical simulations carried out by Le Dizès & Laporte (2002). The divergence pattern we have observed has been previously noted by Pradeep & Hussain (2001), who conducted direct numerical solutions of the bending waves caused by the elliptical instability of a Rankine vortex column. They find that the dipolar pattern in the divergence field is oriented in the direction of compressional strain, as can be seen in their figure 27. This is in agreement with our observations and with the analytical solution of Waleffe (1990) outlined earlier.

4.1.2. *Elliptical instability growth rate*

It was not possible to compute growth rates from the DPIV measurements of the eigenmode since the temporal resolution of the laser was insufficient to resolve the linear growth of the instability. However, we can use existing elliptical instability theory to estimate growth rates. The elliptical instability growth rate $\sigma_e = (9/16)\varepsilon - \nu k_o^2$ is proportional to the value of the strain at the location of maximum vorticity within an unstable vortex core (Julien, Ortiz & Chomaz 2004) minus a viscous contribution. Using the DPIV velocity fields, we have computed ε at the location of maximum vorticity, which usually corresponds to the vortex centre. These strain values represent a five-point average taken around the point of maximum vorticity within the vortex core. The non-dimensional viscous contribution can be estimated from the wavelength measurements shown in § 3 and yields non-dimensional damping values of $\nu k_o^2 T$ between 0.3 and 1. We provide an estimate of the non-dimensional theoretical growth rate $\sigma_e T$ based on the values of the strain at the vortex centre, which is expected to characterize the growth of axial perturbations on the vortex columns. In figure 8 we show the values of $\sigma_e T$ for the same values of Re_v and KC as the sequence in figure 3. We only plot the values of $\sigma_e T$ at locations within the vortex cores since it is well known that the elliptical instability only affects vorticity-dominated regions with closed streamlines. Each core has a single value of $\sigma_e T$ since it is the strain rate at the vortex centre which sets the growth rate of the instability (Julien *et al.* 2004), as explained above. Values as large as $\sigma_e T = 7$ occur, which suggests that infinitesimal perturbations may grow in amplitude by a factor of up to e^7 in an oscillation cycle, assuming linear growth. In § 4.4 we show the time dependence of the quantity $\sigma_e T$ for different cases and compare it with the growth rates of the centrifugal instability, which is explained below.

4.2. *Centrifugal instability*

Another candidate for instability is the centrifugal instability which arises due to an unstable arrangement of angular momentum (Chandrasekhar 1981). A vortex which has a monotonic vorticity distribution is centrifugally stable. In our case, since vorticity is generated continuously at the flap, opposite-signed vorticity may get

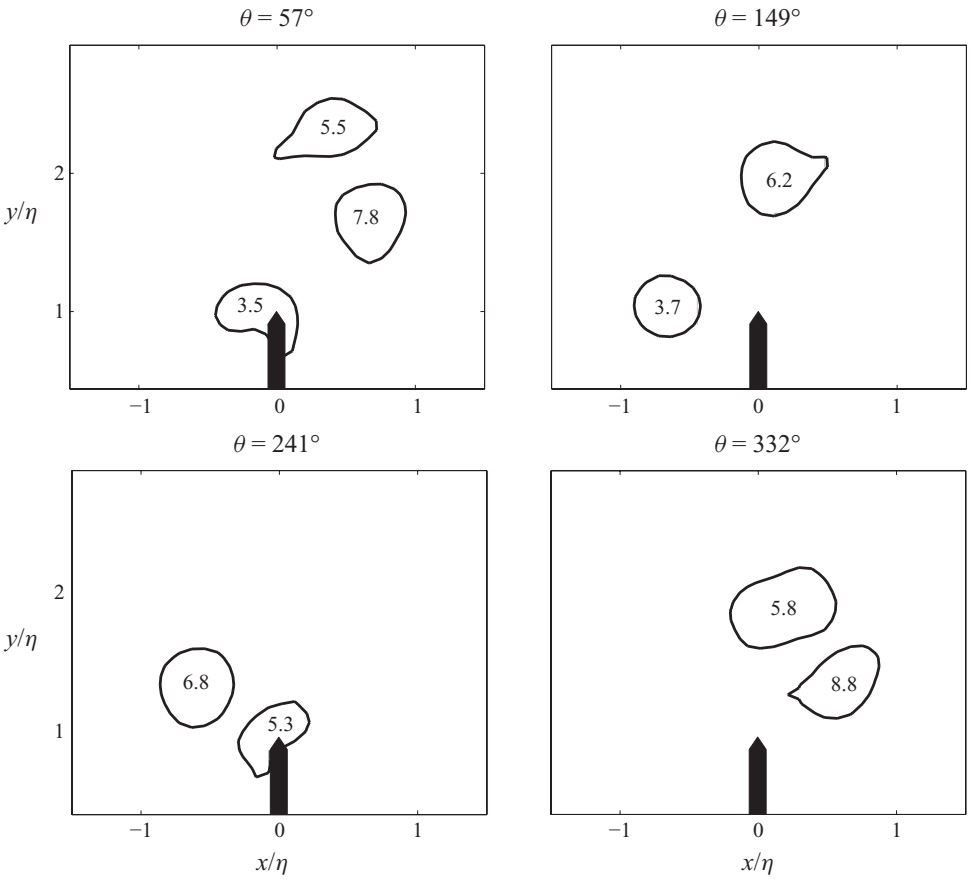

FIGURE 8. Values of the phase-averaged, non-dimensional theoretical growth rates $\sigma_e T = (9/16)\varepsilon T - \nu k_o^2$ for $Re_v = 3800$ and $KC = 1.07$. The black lines denote e-folding vorticity contours to mark the location of the vortex cores.

wrapped around the vortex columns leading to a centrifugally unstable scenario. For an arbitrary 2-D flow, the Rayleigh criterion (Chandrasekhar 1981) for centrifugal instability can be stated in terms of local flow properties as follows (Leblanc & Cambon 1997; Sipp & Jacquin 2000):

$$\Phi = \frac{2\|u\|\omega_z}{R} < 0, \tag{4.6}$$

on a closed streamline ψ_0, where $\|u\|$ is the velocity norm, ω_z is the local vorticity and R is the algebraic radius of curvature of the streamline. The algebraic radius of curvature is given by $R = 1/\kappa$, where κ is the signed curvature of the streamlines. If in some region of the flow there is anticlockwise rotation then $R > 0$, while a region with clockwise rotation has $R < 0$. Equation (4.6) is a sufficient condition for the development of the centrifugal instability in an inviscid planar flow. When $\Phi < 0$, the local vorticity has an opposite sign to the curvature of the streamlines. This can lead to the growth of 3-D short-wave perturbations which are manifested as secondary ring structures in the periphery of the vortex cores.

Note that streamline geometry depends on the frame of reference, and while coherent vortices are expected to show closed streamlines, the vortex pair is propagating at some speed from the flap, so that streamlines appear open in the

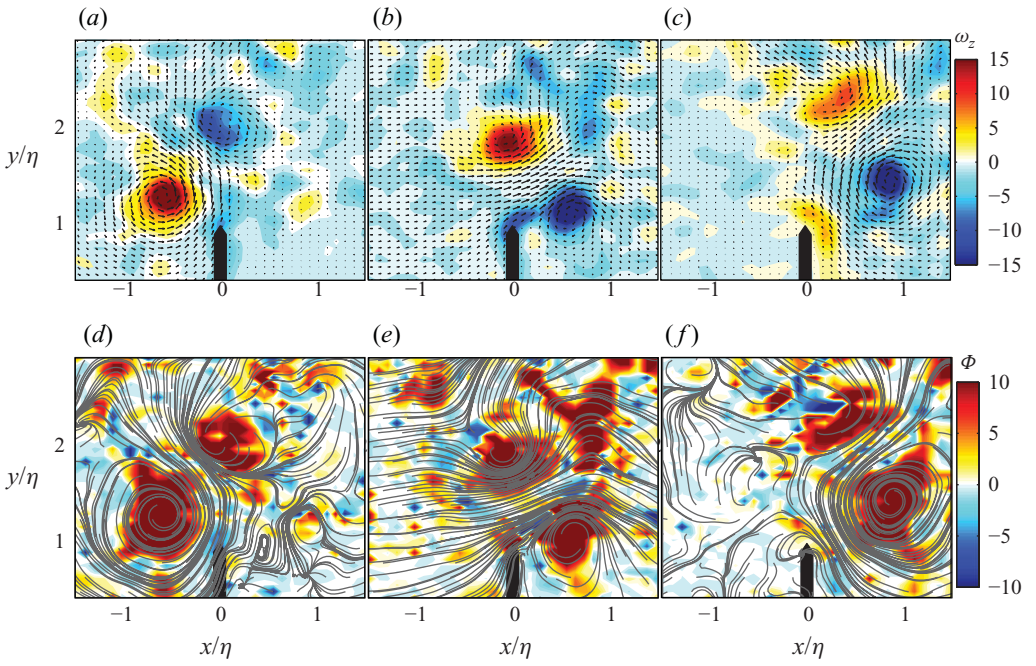

FIGURE 9. Top row: instantaneous dimensional vorticity (contours in s^{-1}) and velocity vectors for oscillation cycle number 13 for $Re_v = 2300$ and $KC = 0.91$ at (*a*) $\theta = 72°$, (*b*) $\theta = 180°$ and (*c*) $\theta = 288°$. Bottom row: (*d*)–(*f*) the dimensional Rayleigh discriminant $\Phi(x, y)$ (contours in s^{-2}) for the same instances as above. The grey lines represent instantaneous streamlines.

frame of reference used here, which is fixed to the flap. If we relax the criteria for closed streamlines in (4.6), we can look for regions which are susceptible to the centrifugal instability using the DPIV velocity fields. This would give a conservative estimate for the degree of instability of these regions. We have computed streamlines and determined their curvature κ as a function of distance along each streamline. From a large quantity of streamlines, we can then interpolate over the DPIV field of view and obtain a 2-D function $R(x, y) = 1/\kappa$, from which we can then determine the value of $\Phi(x, y)$. Figure 9 shows the formation of a typical vortex pair for oscillation cycle number 13 for $Re_v = 2300$ and $KC = 0.91$. The top row depicts the velocity and vorticity fields, while the bottom row shows the value of $\Phi(x, y)$ for each instance, with some streamlines overlaid as black lines. Shades of red are regions for which $\Phi > 0$ and are thus centrifugally stable. Most of the domain appears stable, including the vortex cores. Regions in which $\Phi < 0$, indicating the potential for centrifugal instability, are shown in varying shades of blue. The magnitude of Φ did not vary significantly using a frame of reference fixed to the vortex pairs. The streamlines are shown to visualize which streamlines are approximately closed and which most closely obey the criterion in (4.6). Despite the fact that the function Φ, as a second derivative quantity, is subject to noise, and that it is difficult to identify closed streamlines in which the discriminant is always negative, there are some regions which appear unstable, particularly in the periphery of the cores.

4.2.1. *Centrifugal instability growth rates*

Using the Rayleigh discriminant Φ, we can compute the theoretical centrifugal instability growth rate for the flow. In the limit of very short axial wavelengths and

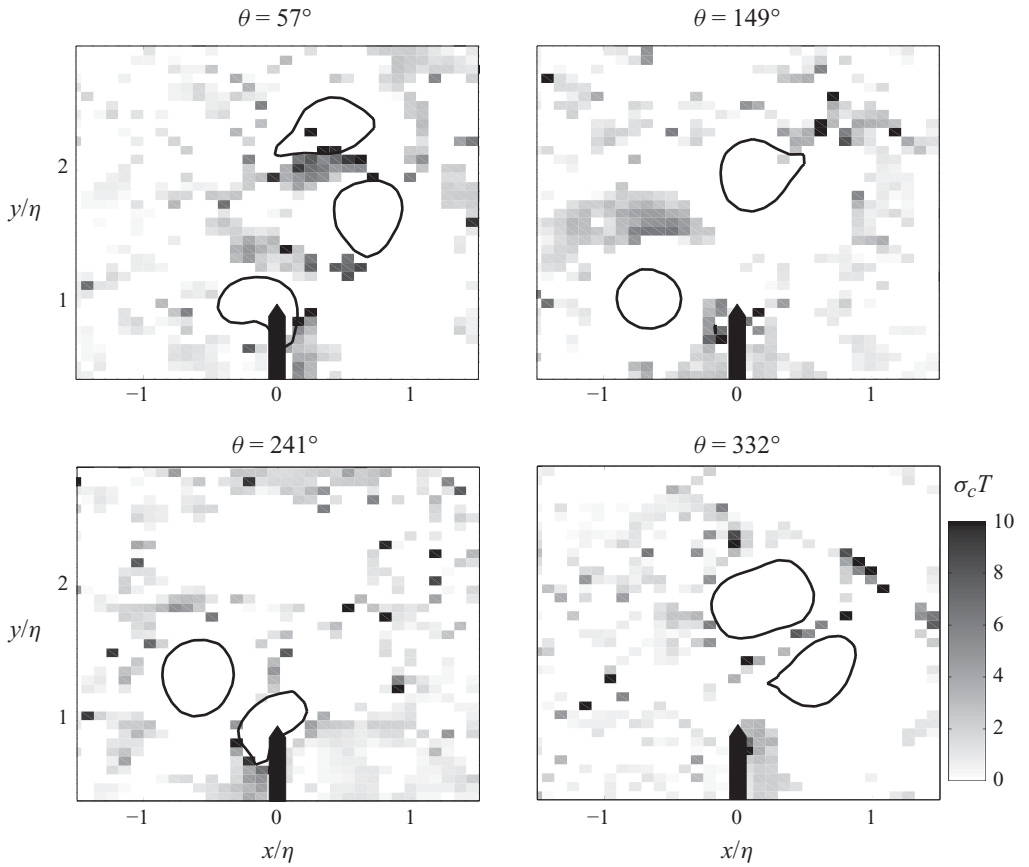

FIGURE 10. Phase-averaged, non-dimensional theoretical growth rates for centrifugal instability, $\sigma_c T = \sqrt{-\Phi} T \in Re$ for $Re_v = 3800$ and $KC = 1.07$. The black lines denote e-folding vorticity contours to mark the location of the vortex cores.

for inviscid flow, the centrifugal instability growth rate is given by $\sigma_c = \sqrt{-\Phi}$ (Bayly 1988; Leblanc & Cambon 1997). In figure 10 we show non-dimensional values of the real part of $\sigma_c T$ for the phase-averaged flow for $Re_v = 3800$ and $KC = 1.07$ at selected phases of an oscillation cycle. Note that the vortex cores are centrifugally stable, while their periphery is unstable. This is because opposite-signed vorticity gets wrapped around the vortex tubes leading to a centrifugally unstable situation in which the local vorticity is opposite to the local streamline curvature. Coherent regions with $\sigma_c T = 10$ or higher can be seen, indicative of the potential for rapidly growing 3-D instabilities. Similar values of $\sigma_c T$ have been observed experimentally by Teinturier *et al.* (2010) in an island wake in a rotating environment, where the period T used in their case corresponds to the vortex shedding period. They find unstable regions in the shear layer emanating from the obstacle as well farther downstream, in the periphery of the unstable vortex columns.

4.3. *Hyperbolic instability*

The strain-dominated regions between the vortex cores are expected to be subject to a hyperbolic instability. This has been observed by Blondeaux *et al.* (2004) to generate complex streamwise structures which wrap around the vortex cores. Julien *et al.* (2004) have investigated the secondary instability mechanisms in the wake of

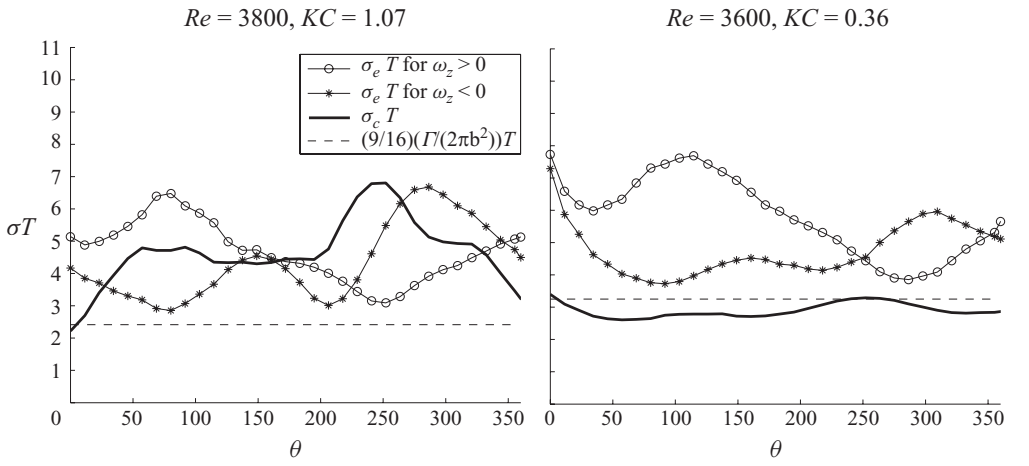

FIGURE 11. Time dependence of phase-averaged, non-dimensional theoretical growth rates for elliptical (○ and ∗ symbols) and centrifugal (solid black line) instabilities for two different cases. The dashed line represents the quantity $(9/16)T\,\Gamma/(2\pi b^2)$ for each case, where Γ and b are the average values for each run.

a flat plate. They find that both the elliptic and hyperbolic instabilities can coexist since they correspond to different regions of the flow. Compared to the elliptical instability, they observe that the hyperbolic instability exhibits transient growth, and that the elliptic instability of the vortex cores sets the global growth rate. In our case, the hyperbolic regions are probably unstable, but the most important instability is expected to be the elliptic instability, since it destabilizes the vortex cores which account for most of the enstrophy and the kinetic energy of the flow.

4.4. *Comparison of growth rates*

Figure 11 shows a comparison of the theoretical phase-averaged elliptical and centrifugal growth rates for two runs at different parameter values as a function of the oscillation phase θ. The first two lines represent the theoretical growth rates based on the measured strain rate and the expected viscous damping for vortices with positive (○ symbols) and negative (∗ symbols) vorticity. The dashed line represents the quantity $(9/16)\varepsilon_t T$, where the quantity $\varepsilon_t = \Gamma/(2\pi b^2)$ is the strain rate that a vortex with circulation Γ would induce at a distance b from that vortex. This indicates the order of magnitude of the expected strain rate that one vortex would induce on the other in a vortex pair, although the real strain rate felt by a vortex is usually up to twice this value (Leweke & Williamson 1998). It is evident that doubling this value would lead to excellent agreement with the values of $\sigma_e T$ shown.

The line with ∗ symbols represents the real part of the phase-averaged theoretical centrifugal instability growth rate $\sigma_c T = \sqrt{-\Phi}\,T$ as a function of θ. This value has been obtained by taking the median of all real values within a distance equal to three times the vortex radius from the centre of each vortex in a given pair. This quantity reaches a maximum close to $\theta = 180°$, which is when the flow reverses and opposite-signed vorticity is generated, which then wraps around the first vortex of each pair, as outlined earlier. It is important to note that the magnitude of $\sigma_c T$ is very similar to those of $\sigma_e T$, indicating that both instabilities appear to grow rapidly and at about the same rate, leading to a very unstable situation which quickly develops into incoherent turbulence.

4.5. *Expected instability wavelengths*

Given the evidence for both elliptical and centrifugal instabilities, it is useful to compare the expected wavelengths for both mechanisms given the observed flow parameters. There is experimental evidence that the axial wavelength of the elliptical instability is of the order of 2–6 times the vortex core size (Leweke & Williamson 1998; Meunier & Leweke 2005), consistent with the observations in figure 5. The axial wavelength for the centrifugal instability is usually smaller than the elliptical instability wavelength at the same Re_v. Kloosterziel, Carnevale & Orlandi (2007) carried out numerical simulations to examine the effects of Reynolds number and stratification on the axial wavelength selection of the centrifugal instability. For zero stratification and $Re_v = 5000$, which is within our parameter range, they find that the axial wavelength is about half the vortex radius ($\lambda/a \approx 1/2$). As the Reynolds number increases, the axial wavelengths become much shorter. They also observe that the radial extent of the overturning motions is restricted to the region in which the Rayleigh discriminant is negative. It is thus likely that the observed wavelengths shown in figure 5 in the range $2 < \lambda/a < 5$ are those associated with the elliptical instability. Since the wavelengths plotted represent those with the highest spectral energy, it is possible that shorter scale instabilities are present, while the elliptical instability produces the largest core displacements which correspond to the dominant spectral peaks. The short wavelengths associated with the centrifugal instability may be more difficult to capture with the DPIV measurements given their very short axial extent, although they are visible in dye visualizations such as those in figure 4. Both instabilities are probably occurring simultaneously, leading to the observed rapid destruction of the vortices.

5. Visualizations of the transition to turbulence

In the previous section, we presented evidence of specific instabilities with similar non-dimensional growth rates which act to destabilize the vortex columns in a very effective way. In this section, we examine the transition to full 3-D turbulence using dye visualizations and DPIV measurements.

5.1. *Dye visualizations*

Dye visualizations of the transition to turbulence for $KC = 0.7$ and $Re_v = 2500$ are shown in figure 12. Red (rhodamine) represents positive spanwise vorticity and green (fluorescein) represents negative spanwise vorticity. The dipole shown corresponds to the second vortex pair after initiation of motion, in which the vortex in red was formed before the vortex shown in green. In figure 12(a), the vortex in red already has perturbations growing on its core. As time goes on, the perturbations on the red vortex grow, while the vortex in green starts to develop waves of its own. By figure 12(c), the perturbations on the red vortex become stretched and wrapped around the vortex in green, while the latter also develops fine-scale structure. Dye from previous and new vortex tubes can be seen in the background. This sequence illustrates an important aspect of the instability of vortex pairs in oscillating flow. One of the vortices will start to feel a strain even before the other vortex has completely formed. Each newly formed vortex tube will become unstable to spanwise perturbations due to the strain induced by the preceding vortex column, which itself has already experienced instability.

5.2. *DPIV observations in a plane parallel to the spanwise vortex tubes*

Velocity measurements in a plane parallel to the dominant spanwise vorticity were conducted to examine the evolution of horizontal vorticity and its relation to vortex

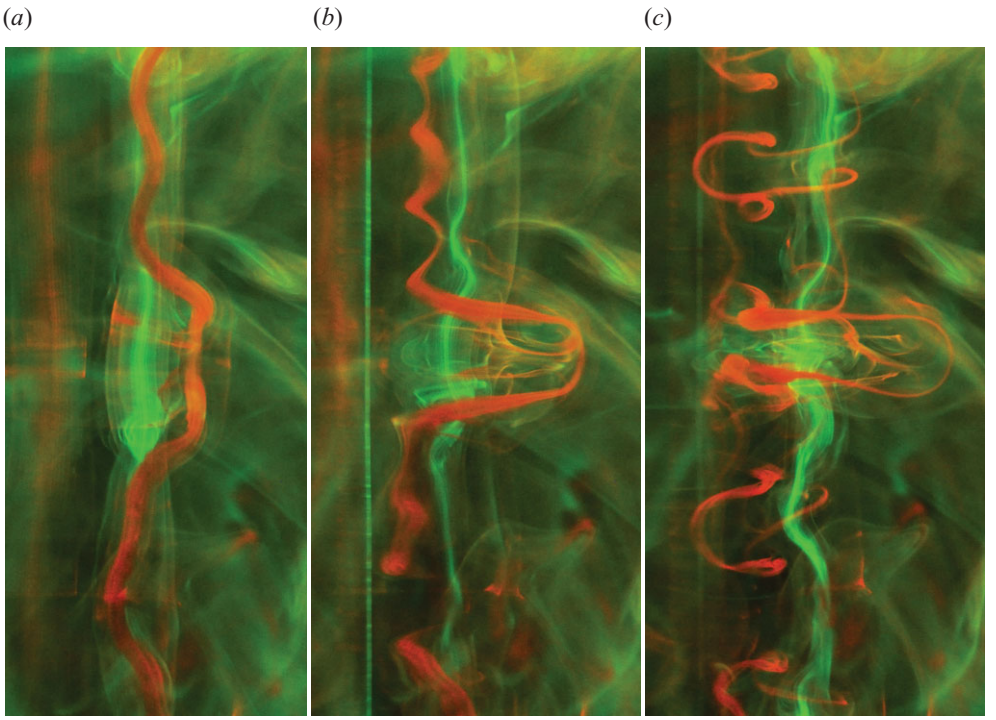

FIGURE 12. Fluorescent dye visualizations for the second oscillation cycle for $KC = 0.7$ and $Re_v = 2500$ at (*a*) $\theta \approx 144°$, (*b*) $\theta \approx 205°$ and (*c*) $\theta \approx 265°$. Red (green) corresponds to positive (negative) spanwise vorticity.

decay. The measurements show a sudden increase in horizontal vorticity at the expense of coherence of the initially spanwise vortices. Figure 13(*a–c*) shows a sequence of the velocity magnitude $\sqrt{v^2 + w^2}$, for the eighth oscillation cycle for parameter values for $KC = 0.27$ and $Re_v = 5740$, starting at $\theta = 200°$, with an interval of 40° between frames. The black rectangle on the left-hand side of each frame denotes the extent in the y/η direction of the flap, but does not imply that the flap was present in that plane when the measurement was obtained. The inset in each frame represents the phase-averaged spanwise vorticity from DPIV measurements of a different experiment at the same parameter values. This vorticity is shown to illustrate the average location of the coherent vortices at the phase at which the instantaneous measurements of the velocity magnitude are shown. The black dashed line represents the approximate location of the vertical slice formed by the laser sheet. It can be seen that, as the vortex pair forms, it propagates away from the boundary; this is evident in both the phase-averaged and instantaneous plots. The older vortex in the pair is contained in the vertical slice, and its core appears sinuously deformed even before it has completely paired with the younger vortex tube, although it is already under the influence of the strain produced by the rolling up of the shear layer at the separation point. In figure 13(*d–f*), we show the instantaneous streamwise vorticity ω_x from the velocity fields shown in figure 13(*a–c*), respectively. In these plots we have used the same colour scale for the vorticity magnitude as the inset plots showing the phase-averaged spanwise vorticity. For frames (*d*) and (*e*) the horizontal vorticity is weak, but in frame (*f*) the horizontal vorticity increases dramatically at the same time that the spanwise coherence in frame (*c*) breaks down.

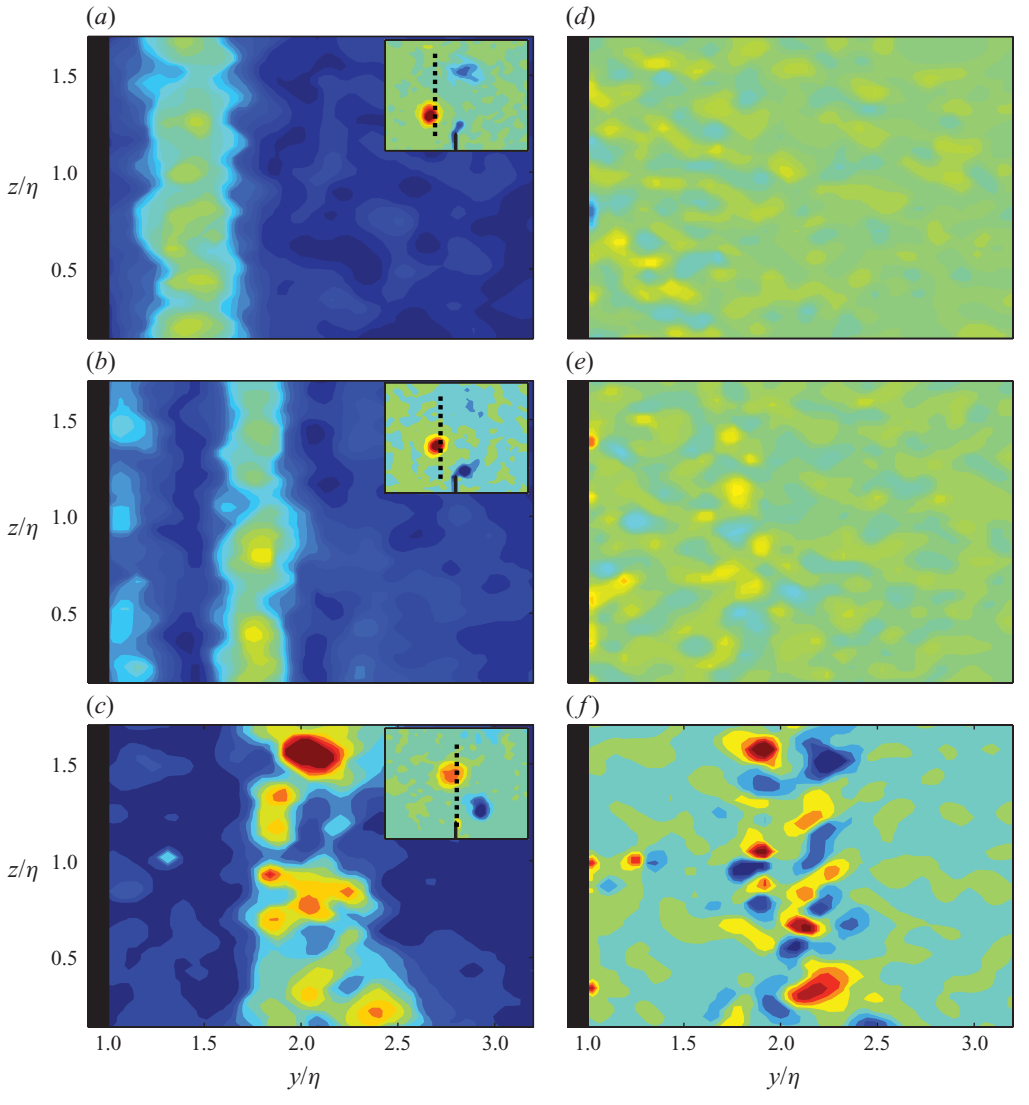

FIGURE 13. Observations of transition to turbulence from DPIV measurements in a vertical plane (VLS), for the eighth oscillation cycle for parameter values for $KC = 0.27$ and $Re_v = 5740$. (*a*)–(*c*) Contours of velocity magnitude $\sqrt{v^2 + w^2}$, starting at $\theta = 200°$, with an interval of 40° between frames. Note the sinuously deformed vortex core in (*a*). The insets represent the phase-averaged spanwise vorticity at the phase of each frame, obtained in a different experiment for the same parameter values. The dashed line indicates the approximate location of the laser sheet. (*d*)–(*f*) Horizontal vorticity ω_x for the snapshots in (*a*)–(*c*), respectively. As mentioned in the text, the colour scale for the values of ω_x is the same as the one used in the insets in (*a*)–(*c*) which show the phase-averaged spanwise vorticity.

The sudden increase in horizontal vorticity is most likely due to the tilting of the spanwise vorticity into the horizontal direction, due to the stretching of the perturbations which initially grew due to the elliptical and centrifugal instabilities. Note that the magnitude of ω_x is equal to or larger than the value of the phase-averaged spanwise vorticity, indicative of strong tilting of vorticity and also of vortex stretching. Alternating positive (red) and negative (blue) values of ω_x are indicative

of streamwise vortex loops which are probably being wrapped around the younger unstable vortex tube. This transition mechanism was observed to be a robust feature and occurred at every cycle, in a qualitatively similar manner for all values of Re_v and KC in the experiments.

6. Vortex decay time scales

The instability mechanisms we have discussed in the preceding sections lead to rapid vortex decay. In all experiments, vortices were observed to last as coherent structures for less than an oscillation period. In this section, we seek to quantify vortex lifetimes by defining a vortex decay time scale, t_d, which characterizes vortex longevity in oscillatory separated flows. This time scale is important since it determines vortex propagation distances and affects boundary layer turbulence.

The Gaussian fitting we have used to obtain vortex parameters such as core size and maximum vorticity is not appropriate to examine vortex decay since it assumes a Gaussian morphology. The vortex dynamics revealed by DPIV measurements indicate that these vortex tubes break down into smaller disorganized scales that cannot be analysed by Gaussian fitting. We now seek a way to quantify the breakdown of scales of the order of the vortex core size into smaller structures, indicative of the transition to three-dimensional turbulence, which eventually leads to energy dissipation.

6.1. *Enstrophy decay*

To quantify vortex decay, we take two-dimensional spectra of the vorticity magnitude within a square of size $8a \times 8a$, where a is the core size of the vortices, obtained from the Gaussian fit described in § 2. The spectral energy at each wavenumber represents the enstrophy density, ω_z^2, at that wavenumber, which we shall denote as Q. The energy is then averaged in space to obtain a distribution of Q within that square as a function of wavenumber. The process is repeated by calculating spectra in squares in a reference frame moving with the vortex pair. The analysis begins as a vortex pair is formed and may extend up to nearly an oscillation period before the vorticity signal is no longer discernible. Time is non-dimensionalized by the oscillation period T, and the time origin, $t/T = 0$, is taken to be the time at which Q reaches a maximum, which typically occurs around $0.75T$ after maximum oscillation amplitude. We then compute the evolution of Q within a wavenumber bandwidth $\Delta k = k_m$ representative of the vortex core size. It is necessary to consider a wavenumber band instead of a discrete wavenumber to take into account viscous effects which may tend to distribute enstrophy to lower wavenumbers.

For a given vortex and within a wavenumber bandwidth $\Delta k = k_m$, however, viscosity can only redistribute vorticity so that the integrated energy will remain approximately the same. The temporal distribution of enstrophy density, $Q_m(t)$, within that wavenumber band is given by

$$Q_m(t) = \int_{k_m - 1/2k_m}^{k_m + 1/2k_m} Q(k, t)\, \mathrm{d}k. \tag{6.1}$$

In figure 14(a), we show normalized values of $Q_m(t)$ for several vortex pairs for $Re_v = 1240$ and $KC = 0.9$. It can be seen that $Q_m(t)$ decreases steadily with time, almost vanishing completely in a time interval $t/T = 0.8$. All vortex pairs are observed to follow a similar decay in $Q_m(t)$, which confirms the repeatability of vortex instability and decay over several cycles for a single experiment. It should be noted that this

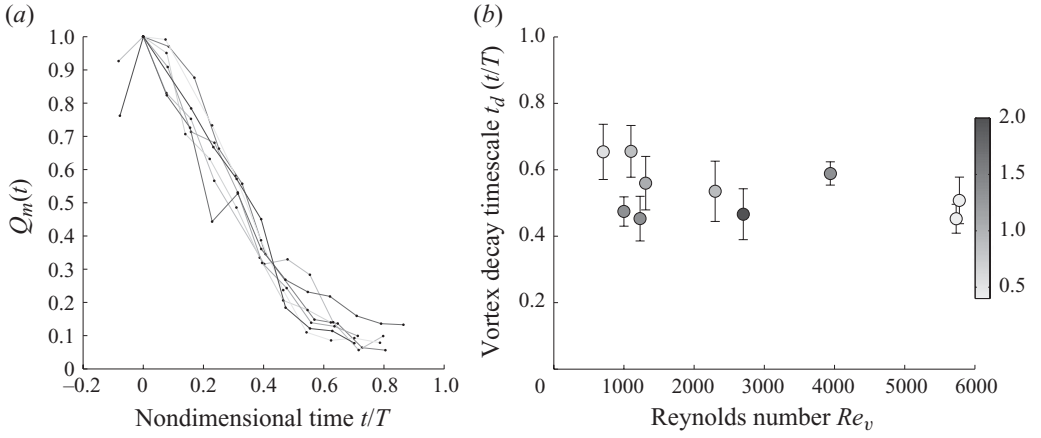

FIGURE 14. (*a*) Distribution of enstrophy density $Q_m(t)$ within a bandwidth Δk for $Re_v = 1240$ and $KC = 0.9$. Each coloured line represents $Q_m(t)$ for a single vortex pair. (*b*) Non-dimensional vortex decay time scale t_d as a function of Re_v. Error bars denote one standard deviation, and the grey shade of each symbol represents the value of KC for that experiment.

decay reflects the large-scale decay of the vortex columns and does not necessarily reflect energy dissipation at the viscous scales.

We now define a vortex decay time scale as the time it takes for $Q_m(t)$ to reach a value of e^{-1} times the maximum energy during the vortex pair's lifetime. This time scale represents the decay of the vortex pair collectively and does not represent the decay of individual vortices. The non-dimensional time t_d is found by linear interpolation, with the calculation carried out for several experiments at different values of Re_v and KC. Only experiments with oscillation periods larger than 3 s have been used in the calculation, since the DPIV sampling frequency is approximately 3.4 Hz. This was necessary in order to have at least 10 data points in a single oscillation period T, so that the vortex lifetimes are adequately resolved in time. Vortex pairs in the experiments with $T < 3$ s were observed to break down in a time interval similar to the experimental runs discussed below.

In figure 14(*b*), we show values of t_d for several experiments, with error bars which denote one standard deviation. It is clear that t_d does not vary significantly with Re_v, and that vortex pairs never survive longer than an oscillation cycle, as is also evident in figure 14(*a*). This has implications related to the vertical extent of rough oscillating boundary layers at low KC, since the propagation distance of vortex pairs will be strongly limited due to their rapid demise.

The observation that t_d does not vary greatly with increasing Re_v highlights the fact that the three-dimensional elliptical and centrifugal instabilities are very effective in breaking down vortex columns, even at relatively low values of Re_v. Vortex pair formation is a common feature of oscillating flow past a rough seabed at low values of KC. For oscillating flow past vortex ripples at low KC, vortex pairs are expected to decay quickly and, as was observed in the preceding sections, they are unlikely to propagate distances larger than $y/\eta = 3$ from the seabed. Different oscillation periods were used for similar values of Re_v, yet vortex decay time scales consistently scale with the oscillation time. This indicates that vortex longevity is greatly influenced by vortex interactions, which provide the necessary strain fields and residual opposite-signed vorticity to lead to instability and turbulence via the elliptical and centrifugal instabilities.

7. Conclusions

We have examined the three-dimensional dynamics of coherent vortices in an oscillatory separated flow. Flow visualization and digital particle imaging velocimetry have been used to elucidate the vortex dynamics. The flow is dominated by the unidirectional propagation of a new vortex pair at each cycle. The direction of propagation of the vortex pair depends on the initial conditions, and once the pattern is established it remains stable for all subsequent cycles. The vortex pairs were observed to break down rapidly, which limits the distance to which they can propagate as coherent structures under mutual advection.

An elliptical instability has been observed which breaks down the spanwise coherence of these vortices. The physical mechanism for instability is the stretching of perturbation vorticity by the strain field that vortices induce on each other. This instability leads to growing spanwise undulations which are axially periodic. The spatial structure of the instability was identified in the divergence field and showed good agreement with elliptical instability theory. At any instant, the growth of the inertial waves is more advanced in one of the vortices, because one vortex forms before the other, and may become unstable before the other vortex of each pair is formed completely. These results have thus identified the spatial structure of the perturbation field associated with the elliptical instability in a realistic, vortex-dominated, open flow, without artificial spanwise forcing.

We also identify regions in which the flow may be centrifugally unstable. In this complicated flow, vorticity is generated continuously throughout the oscillation cycle, and vorticity of opposite sign gets wrapped around the vortex columns, leading to a centrifugally unstable flow. A comparison of the theoretical growth rates, which have been estimated based on the flow properties extracted from the DPIV measurements, suggests that the instabilities grow rapidly. Both instabilities have comparable growth rates, which indicates that both are simultaneously present and lead to the observed destruction of the vortices and the transition to turbulence. Although the interaction between the two instability modes was not analysed, we can hypothesize that the centrifugal instability may reinforce the elliptical instability by providing finite amplitude perturbations that can grow rapidly via the vortex stretching mechanism characteristic of the elliptical instability. Further laboratory and numerical studies are necessary to better understand the feedback between the instability modes.

A vortex decay time scale is used to quantify the destruction of the vortices. The results confirm that the vortex pairs are short-lived and do not survive more than an oscillation period T after they are formed. This has important implications for rough oscillating boundary layers, since the short vortex lifetimes limit the height to which vortex pairs can propagate and affect the boundary layer structure.

This study was supported by the National Science Foundation under grant OCE–04255893. David 'Araña' Carrero provided invaluable help with the experimental set-up, and Rudolf Kloosterziel provided useful comments which improved the quality of the article. Comments from two anonymous reviewers greatly improved an earlier draft of the paper and, in particular, were helpful in identifying the potential role of the centrifugal instability.

REFERENCES

Bayly, B. J. 1986 Three-dimensional instability of elliptical flow. *Phys. Rev. Lett.* **57** (17), 2160–2163.

Bayly, J. 1988 Three-dimensional centrifugal-type instabilities in inviscid two-dimensional flows. *Phys. Fluids* **31**, 56–64.

Blondeaux, P., Scandura, P. & Vittori, G. 2004 Coherent structures in an oscillatory separated flow: numerical experiments. *J. Fluid Mech.* **518**, 215–229.

Chandrasekhar, S. 1981 *Hydrodynamic and Hydromagnetic Stability*. Dover.

Craik, A. D. D. & Criminale, W. O. 1986 Evolution of wavelike disturbances in shear flows: a class of exact solutions of the Navier–Stokes equations. *Proc. R. Soc. Lond.* A **406**, 13–26.

Eloy, C., Le Gal, P. & Le Dizès, S. 2000 Experimental study of the multipolar vortex instability. *Phys. Rev. Lett.* **85** (16), 3400–3403.

Fincham, A. & Spedding, G. 1997 Low cost, high resolution DPIV for measurement of turbulent fluid flow. *Exp. Fluids* **23**, 449–462.

Graham, J. M. R. 1980 The forces on sharp-edged cylinders in oscillatory flow at low Keulegan–Carpenter numbers. *J. Fluid Mech.* **97**, 331–346.

Julien, S., Ortiz, S. & Chomaz, J.-M. 2004 Secondary instability mechanisms in the wake of a flat plate. *Eur. J. Mech.* B: *Fluids* **23**, 157–165.

Kelvin, Lord 1880 Vibrations of a columnar vortex. *Phil. Mag.* **10**, 155–168.

Kloosterziel, R. C., Carnevale, G. F. & Orlandi, P. 2007 Inertial instability in rotating and stratified fluids: barotropic vortices. *J. Fluid Mech.* **583**, 379–412.

Krstic, R. V. & Fernando, H. J. S. 2001 The nature of rough-wall oscillatory boundary layers. *J. Hydraul. Res.* **39**, 655–666.

Landman, M. J. & Saffman, P. G. 1987 The three-dimensional instability of strained vortices in a viscous fluid. *Phys. Fluids* **30**, 2339–2342.

Le Dizès, S. & Laporte, F. 2002 Theoretical predictions for the elliptical instability in a two-vortex flow. *J. Fluid Mech.* **471**, 169–201.

Leblanc, S. & Cambon, C. 1997 On the three-dimensional instabilities of plane flows subjected to Coriolis force. *Phys. Fluids* **9** (5), 1307–1316.

Leweke, T. & Williamson, C. H. K. 1998 Cooperative elliptic instability of a vortex pair. *J. Fluid Mech.* **360**, 85–119.

Longuet-Higgins, M. S. 1981 Oscillating flow over steep sand ripples. *J. Fluid Mech.* **107**, 1–35.

Mei, C. C. & Liu, P. L. 1993 Surface waves and coastal dynamics. *Annu. Rev. Fluid Mech.* **25**, 215–240.

Meunier, P. & Leweke, T. 2003 Analysis and treatment of errors due to high velocity gradients in particle image velocimetry. *Exp. Fluids* **35**, 408–421.

Meunier, P. & Leweke, T. 2005 Elliptic instability of a co-rotating vortex pair. *J. Fluid Mech.* **533**, 125–159.

Meunier, P., Leweke, T., Lebescond, R., Van Aughem, B. & Wang, C. 2004 *DPIVsoft User Guide*. IRPHE.

Moore, D. W. & Saffman, P. G. 1975 The instability of a straight vortex filament in a strain field. *Proc. R. Soc. Lond.* A **346**, 413–425.

Nichols, C. S. & Foster, D. L. 2007 Full-scale observations of wave-induced vortex generation over a rippled bed. *J. Geophys. Res.* **112** (C10015).

Pradeep, D. S. & Hussain, F. 2001 Core dynamics of a strained vortex: instability and transition. *J. Fluid Mech.* **447**, 247–285.

Scandura, P., Vittori, G. & Blondeaux, P. 2000 Three-dimensional oscillatory flow over steep ripples. *J. Fluid Mech.* **412**, 355–378.

Singh, S. 1979 Forces on bodies in oscillatory flow. PhD thesis, University of London.

Sipp, D. & Jacquin, L. 2000 Three-dimensional centrifugal-type instabilities of two-dimensional flows in rotating systems. *Phys. Fluids* **12** (7), 1740–1748.

Tao, L. & Thiagarajan, K. 2003 Low KC flow regimes of oscillating sharp edges I. Vortex shedding observation. *Appl. Ocean. Res.* **25**, 21–35.

Teinturier, S., Stegner, A., Didelle, H. & Viboud, S. 2010 Small-scale instabilities of an island wake flow in a rotating shallow-water layer. *Dyn. Atmos. Oceans* **49**, 1–24.

Tsai, C.-Y. & Widnall, S. E. 1976 The stability of short waves on a straight vortex filament in a weak externally imposed strain field. *J. Fluid Mech.* **73**, 721–733.

Waleffe, F. 1990 On the three-dimensional instability of strained vortices. *Phys. Fluids* **2** (1), 76–80.

Williams, J. J., Metje, N., Coates, L. E. & Atkins, P. R. 2007 Sand suspension by vortex pairing. *Geophys. Res. Lett.* **34**.